Aerospace Science and Technology 180 (2027) 114154

Contents lists available at ScienceDirect

Aerospace Science and Technology

journal homepage: www.elsevier.com/locate/aescte

Original article

Predictive models of acoustic dynamics of a contra-rotating propeller UAV during ascent, hover, and descent

Camilo I. Andino Cappagli *, Alireza Amiri-Simkooei , Mirjam Snellen

Operations and Environment, Faculty of Aerospace Engineering, Delft University of Technology, Delft, Kluyverweg 1, South Holland, 2629HS, The Netherlands

ARTICLE INFO

Communicated by Dr. Qu Qiulin

Keywords:
Drone noise
Multi-rotor UAV
Machine learning predictive models
On-field array-based noise measurements
Contra-rotating propeller
Telemetry analysis

ABSTRACT

This work explores the development of predictive models for the noise of a contra-rotating propeller (CRP) drone operating under real flight conditions. Using supervised machine learning techniques, empirical models are established to predict the time-dependent behavior of the overall sound pressure level (OSPL) and its A-weighted counterpart (OASPL) during ascent, hover, and descent manoeuvres. Experimental array-based acoustic data and comprehensive telemetry recorded during outdoor flight tests are employed to train and optimize the models, and subsequently assess their performance on unseen data. A set of meaningful telemetry-based observables is used as candidate input features for predicting both acoustic signals. These observables reflect the underlying flight dynamics and the environmentally induced perturbations to the vehicle dynamics. Statistical methods are employed to quantify the importance of each telemetry variable in predicting the acoustic signals, indicating that only a small set of variables is needed to achieve high predictive accuracy for both OSPL and OASPL using a reduced set of variables. Comprehensive evaluation of the models is conducted on unseen and highly variable acoustic data. The results reveal that the proposed models can accurately capture the time-dependent evolution of OSPL and OASPL during the studied manoeuvres. These findings provide a useful preliminary predictive tool for noise prediction during real UAV operations, as well as for noise-based trajectory optimization of single-UAV operations.

1. Introduction

The rapid expansion of unmanned aerial vehicle (UAV) operations in logistics, inspection, and urban mobility has introduced new challenges related to vehicle performance, control, and environmental integration. Addressing these challenges allows a variety of sectors in the public and private spheres to sustainably exploit the multiple advantages UAVs offer. For example, they have been successfully tested as fast delivery systems for medical supplies or equipment during emergencies, where the drone's ability to rapidly navigate difficult terrain and avoid land obstacles can be critical [1]. Their reconnaissance capabilities are also valuable during emergencies and natural disasters where fast and versatile aerial assessment is needed, as well as in search-and-rescue (SAR) operations [2]. In commercial settings, drones can also be used as payload delivery systems, reducing emissions typically associated to other types of transportation. However, as low-altitude aerial operations become more frequent and distributed, understanding and managing UAV noise has become a prerequisite for their sustainable integration into the urban airspace [3–5].

Drone noise has become an important research topic due to the appearance of different UAV sizes and configurations, as well as new UAM (Unmanned Aerial Mobility) vehicle concepts and prototypes. Most existing research has primarily addressed aeroacoustic studies at the subsystems level [6,7] or on full UAVs operating under steady operating conditions [8,9]. These studies are crucial for understanding the physical principles of sound generation and its different characteristics. However, the sound is modified when interactions between subsystems are addressed [10,11], making the scenario closer to the complete system representation. For multi-rotor UAVs, the noise is mostly dominated by strong tonal components at the Blade Passing Frequency (BPF) and its harmonics [12,13]. This is also relevant for eVTOL-capable fixed-wing drones. At low rotational Mach numbers and for thin blades, the dominant tonal noise generating mechanism stems from the unsteady loading by the blades [12,14–18].

When full UAV systems are considered, the rotor type, airframe configuration, and flight procedure all influence the characteristics of the noise [4,11]. Depending on these factors, broadband noise could also appear and even dominate at different frequency ranges. This

* Corresponding author.
E-mail address: c.i.andinocappagli@tudelft.nl (C.I. Andino Cappagli).

https://doi.org/10.1016/j.ast.2026.114154
Received 16 December 2025; Received in revised form 26 October 2026; Accepted 26 October 2026
Available online 29 October 2026
1270-9638/© 2026 The Authors. Published by Elsevier Masson SAS. This is an open access article under the CC BY license (http://creativecommons.org/licenses/by/4.0/).

increasing complexity, arising from the interaction between different subsystems and with the local flow dynamics, makes the accurate prediction of drone noise under real operating conditions highly challenging.

Furthermore, variations in thrust, and consequently propeller rotational speeds, are often needed in response to environmental perturbations such as wind gusts.

Several recent studies have focused on acoustic characterization of complete UAVs performing specific maneuvers [10,19–23]. These works investigated different drone types and configurations under controlled conditions. In [20], the authors conducted a series of acoustic characterizations of different drones and their radiation pattern, and studied trends and scalings with operational parameters. Among their findings, they reported strong evidence of an inverse relation between the A-weighted sound pressure level and the advance ratio when comparing identical flight patterns across different UAVs. Their comparative analysis also indicated that increases in advance ratio can serve to compensate increments in sound pressure level caused by a higher take-off weight (TOW). They also found correlations indicating that the A-weighted Sound Exposure Level scales with both TOW and vehicle speed. In [10], the tonal component of the noise was found to be heavily affected by UAV operation and orientation. For horizontal flight, the two dominant BPF tones of the tested UAV converged during the acceleration phase and diverged during the deceleration phase. In [19], frequency and amplitude variations were observed in the spectrogram during take-off and vertical flight, which corresponded to specific dynamics of the propeller system. The above findings highlight the potential of studying the acoustic output of full UAVs during real maneuvers using flight-dynamics-based observables.

Based on this potential, the current study presents a series of experimental flight tests and develops empirical models that capture the interaction between UAV telemetry variables (describing the propeller rotational speeds and drone position) and the noise output. The main objective is to explore and establish effective relations between telemetry-based variables and acoustic signals. Using these relations, we develop a series of empirical models as an initial tool to predict UAV acoustic performance. As a first step, the acoustic output is described using simple yet important metrics: OSPL and OASPL. The experimental flight tests and models will focus on a set of operations, including ascent, hover, and descent.

The objectives of this work are three-fold. i) We develop a functional predictive model for drone noise using an extensive experimental campaign, conducted to provide comprehensive acoustic and telemetry data from full UAV operations. ii) A series of post-processing tools is built to enhance data quality and extract meaningful observables representative of the acoustic dynamics and the underlying flight behavior. iii) Using this set of input variables (and its reduced subset), an appropriate machine learning model is optimized, on training data, and tested, on unseen data, to predict OSPL and OASPL time series during ascent, hover, and descent maneuvers. The resulting empirical models establish a preliminary tool to assess drone noise during real operations, and offer a framework for generalization to other drones and maneuvers, which allows predictions in broader operational conditions. Beyond prediction, this framework also highlights the key telemetry variables that drive OSPL and OASPL dynamics, demonstrating its benefit as a fast data-driven method to identify influential control parameters.

Section 2 presents the experimental setups, which includes flight procedures, equipment, and UAV specifications. This section also explains the beamforming-based methods employed to back-propagate the acoustic signals to the UAV location, synchronize the telemetry with noise measurements, and improve the GPS-derived positions. Section 3 reports the results, starting with an initial analysis of the OSPL and OASPL signals from the operations. We then describe the development of a machine-learning model to predict the OSPL and OASPL as a function of telemetry-based observables. This is performed based on all available data, recorded at each time instance as a time series. Finally, Section 4 discusses the contributions and limitations, as well as the future perspectives arising from this work.

2. Methods

2.1. Experimental flight tests

A series of flight tests were conducted to measure the noise emitted by a drone while it performed numerous maneuvers in outdoor conditions, reflecting realistic environmental situations. For this work, we focused on operations comprising ascent, hover, and descent, thereby allowing the UAV to move only along an approximately vertical line. Different repetitions of the operations were performed at different Vertical Take-off and Landing (VTOL) sites, changing the azimuthal orientations and ranges relative to the array. The experiments took place in an airfield located at Vrátkov-Český Brod, Czechia during April 2024. The airfield was located far from population centers, having only a rarely used single road located nearby. During the three days experimental campaign, very little wind was experienced on the site. The airspace during the days was quiet, with around 10 to 15 aircraft flyovers at cruise altitude each day. The tests measured for the current work were not taking longer than five minutes per flight, avoiding spurious noise contributions to the measurements.

The flight tests analyzed were performed by a contra-rotating propeller (CRP) quadcopter drone denominated Gorgon X8, developed by Agent Fly Technologies, who in addition provided the pilots and logistics on the site. The UAV can be observed in Fig. 1c. The drone has dimensions $100 \times 95 \times 31$ cm, a take-off weight of 12.96 kg and has systems that record different types of data, such as GPS position, RPM activity of individual rotors, thrust, and attitude dynamics data.

The acoustic data was recorded using a microphone array with 64 microphones, a diameter of 4 m and a sampling frequency of 62.5 kHz, see Fig. 1b. The VTOL and array positions are shown in Fig. 1a.

A protector and a foam were placed underneath the array to reduce ground reflections, and secondary foam was added to the central microphones to avoid secondary reflections from the array structure. Windshields were placed over all microphones.

The flight tests consisted of the drone taking off, ascending to a predefined height above ground level (AGL), hovering for a period between 15 to 20 s, and ascending again to hover at the next height for the same period of time. The pattern was repeated such that four hovers were performed per operation, at 10 m, 30 m, 50 m, and 70 m, after which the drone descended continuously until landing in the same take off position, hence the trajectory is entirely vertical. Each operation was manually piloted to allow for corrections in the duration of the hovers as strong wind gusts could perturb a given hover maneuver. In some of these cases, this could be detected by either the pilot or the controllers during flight, who could decide to maintain the hover for longer. The altitude profile as a function of time for one of such tests is shown in Fig. 2.

This was repeated five times, with varying take off positions by changing the azimuthal orientation and range relative to the array to assess the validity of the later backpropagation to the source. Fig. 1 shows the different take off positions relative to the microphone array. A nearby weather station provided data on temperature, relative humidity, and average wind speed, which are shown in Table 1 for each of the five operations.

2.2. GPS accuracy enhancement and telemetry synchronization

The telemetry during flight and the acoustic data are not recorded by the same data acquisition system. This poses the challenge of synchronizing both data sources to ensure a correct combination of acoustic and flight dynamics variables.

To solve this, we applied beamforming to the acoustic array data using the central eight microphones to generate an independent

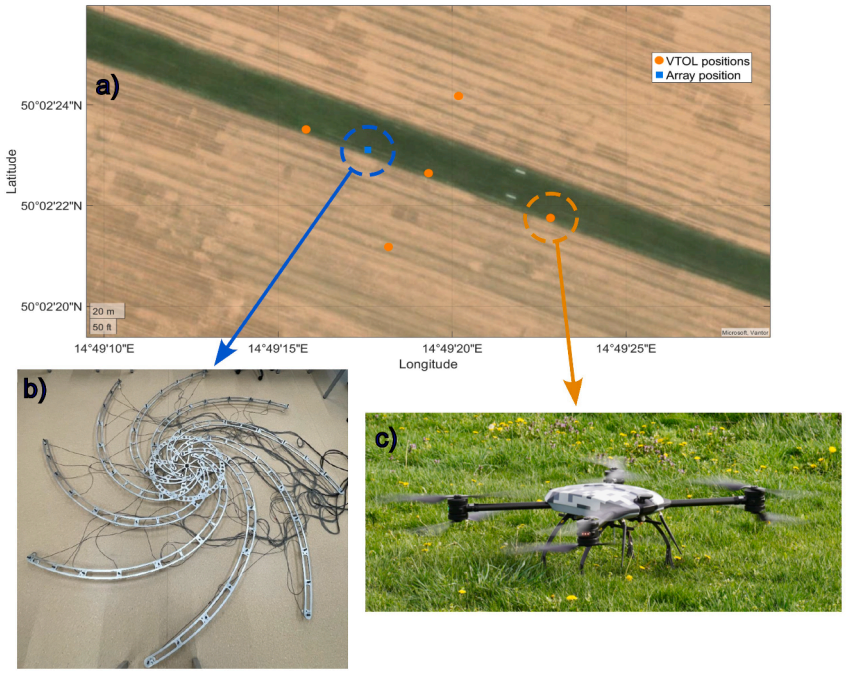


Fig. 1. (a) Take off/landing and main array positions of each of the described operations. (b) Microphone array and structure. The array is comprised of 64 microphones and a diameter of 4 m, with a sampling frequency of 62.5 kHz. (c) Picture of the studied X8 drone Gorgon. At each VTOL position, the drone performed the operation whose altitude profile is shown in Fig. 2, while the microphone array recorded the acoustic signals.

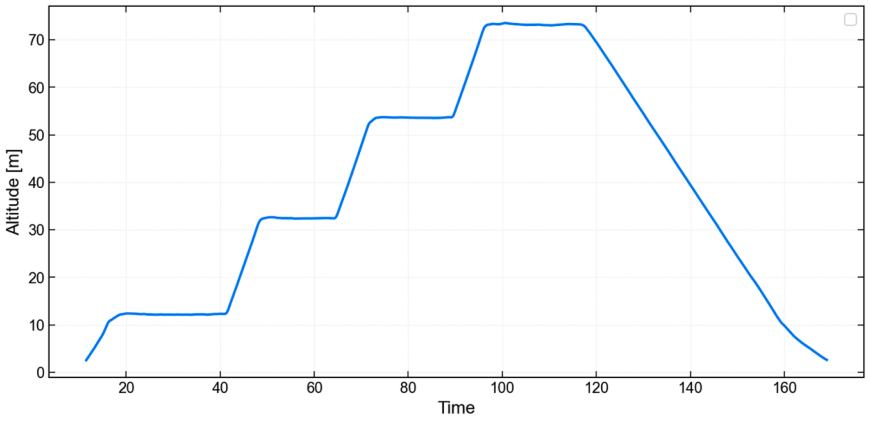


Fig. 2. Altitude profile for a single ascent-hover-descent operation.

Table 1
Weather data during each operation.

Operations	Wind speed [m/s]	Wind direction [deg (direction)]	Relative humidity [%]	Temperature [deg. c]
1	2.2	126 (SE)	43	25.9
2	2.9	126 (SE)	42	25.8
3	3.3	127 (SE)	43	25.4
4	3.5	127 (SE)	45	25
5	3.5	127 (SE)	45	25

reconstruction of the drone trajectory and systematically use it to reconstruct more accurately the relative (to the array) drone locations, which in turn, can be used to synchronize all the telemetry data.

For the beamforming step a differential evolution (DE) algorithm was employed: instead of using an exhaustive grid-based search for identifying the source position from the acoustic array data, the DE algorithm works with populations of potential source positions, steering over a series of so-called 'generations' toward the source position that provides an optimal match between measured and modeled phase variation over the array. The acoustic measurement time series is divided in small snapshots and the DE approach is applied to the data of each snapshot separately. The energy function to be optimized by DE is defined as:

$$E = -\sum_i |H_i| \tag{1}$$

where the index i specifies the frequency considered and where

$$H_i = \mathbf{p}^*(f_i) \cdot \exp(-2\pi j f_i \boldsymbol{\tau}) \tag{2}$$

with the asterisk $(\cdot)^*$ denoting the complex conjugate transpose, $\mathbf{p}$ is the vector containing the Fourier transforms of the data measured at the array for all microphones and the snapshot selected, and $\exp(-2\pi j f_i \boldsymbol{\tau})$ is the vector containing the modeled phase variation over the array, with $\boldsymbol{\tau} = ||\mathbf{r}_A - r_s||/c$ the time delays between the microphone positions $\mathbf{r}_A$ and the scan position, i.e., potential source position, r_s.

As indicated earlier, the energy function, Eq. (1), is not evaluated at predefined scan grid points, but instead scan positions are evolved in a genetic tournament within the differential evolution algorithm until the energy function is minimized (as defined by the minus sign in Eq. (1)). The state that minimizes the energy function is the resulting GPS-independent trajectory $\mathbf{r}_{ac} = (r_{ac}, \theta_{ac}, \phi_{ac}) = \arg\min_{\mathbf{r}} E,$. Here r_{ac} indicates the distance between the array and the drone, θ_{ac} indicates the angle of the drone relative to the array plane (horizontal), and ϕ_{ac} indicates the angle of the drone in the horizontal plane. The subscript 'ac' indicates that the value is obtained from the DE estimations. Accurate estimates for the range r_{ac} can only be obtained for cases with the drone close to the array.

These estimates are used to synchronize the telemetry and acoustic data streams. A first visual-based estimation of shifts (time and angular position shifts), $\Delta\phi_0$ and Δt_0, is generated through aligning the drone location estimates obtained from beamforming and from the drone GPS, accounting for the travel time of the sound to the array. $\Delta\phi_0$ reflects the orientation of the array in the drone GPS coordinate system. It was found that by only accounting for these shifts, both trajectories did not yet coincide. Therefore, the DE algorithm was employed again but with a modified energy function, built to quantify the match of both trajectories, as:

$$E(\delta_t, \delta_\phi, \delta_x, \delta_y, \delta_z) = Median\left(\sqrt{(\theta_{ac}(\delta_t, \delta_\phi, \delta_x, \delta_y, \delta_z) - \theta_{gps})^2 + (\phi_{ac}(\delta_t, \delta_\phi, \delta_x, \delta_y, \delta_z) - \phi_{gps})^2}\right) \tag{3}$$

where the median is taken to make the energy function less sensitive to outliers. The unknowns δ_t, δ_ϕ, δ_x, δ_y and δ_z are found by minimizing Eq. (3) and reflect a finetuning of the time offset (δ_t), a finetuning of the array angle (δ_ϕ) and changes in the relative position of the drone to the array (δ_x, δ_y and δ_z). Importantly, there is no assumption of ground truth from the acoustic nor GPS data, i.e., only the relative positions of the drone to the array are determined.

With the location of the drone relative to the array known, the array data is used to steer the array to the drone position and to calculate the source auto-power for each trajectory point and frequency f as [24]:

$$A = \frac{1}{2}\frac{\mathbf{g}^* \mathbf{p}\mathbf{p}^* \mathbf{g}}{||\mathbf{g}||^4} \tag{4}$$

where the elements m of the steering vector $\mathbf{g}$ are defined as

$$g_m = (1/r)\exp(-2\pi j f \tau_m) \tag{5}$$

and r indicates the distance from the center of the array to the instantaneous drone location.

The monopole assumption is adopted as a simplified, effective source model for the beamforming procedure, with allows for the directional acoustic levels to be determined. The resulting levels should be interpreted as a monopole-equivalent estimates of the back-propagated far-field acoustic signals measured on the ground rather than a representation of the total acoustic power of the UAV. In other words, the beamformed signal represents the field that when forward-propagated yields the far-field acoustic signals measured by the array, without the ground effects. Due to the small aperture covered by the microphones used for obtaining the beamformed signal, the drone directivity is assumed equal for all microphones per time snapshot.

In this way, the beamformer generates spectrogram data at the source location, thereby producing spectrogram data with improved signal-to-noise ratio compared to data from a single microphone. (The correction for loss due to atmospheric absorption is applied after evaluating Eq. (4)). By following this approach, also the contributions from ground reflections observed in the single-microphone data were significantly reduced. Overall, around 2000 time instances were present in the beamformed data of each operation, adding up to 10000 samples total.

DE is a stochastic method, meaning that each run can result in slightly different estimates for the shifts. For the case considered, the DE settings were such that all runs converged to the same solution. However, by considering less generations, variability was found. This variability is considered representative of the maximally expected uncertainties in the shifts (see Eq. (3)). In total hundred slightly different estimates for the shifts have individually been used for synchronizing the array and telemetry data and for subsequently estimating the beamformed spectrogram, and OSPL and OASPL. From this, the standard deviation at each signal index was calculated, resulting in a signal describing the variance. This analysis resulted in a variable standard deviation; when the elevation angle is the smallest, meaning that the drone is closest to the ground, the maximum standard deviation was found to be approximately 1.2 dB (dBA, in the OASPL case), and 0.1 dB (dBA) when the drone was at its maximum altitude, and thereby at the maximum angle of elevation.

2.3. Machine learning models

To generate data-driven models capable of linking the synchronized telemetry variables with the acoustic dynamics, several regression models were studied; specifically, Random Forest, Histogram Gradient Boosting, Support Vector Machines, and Multilayer perceptrons [25–27]. Histogram-based Gradient Boosting Regression (HGBR) models were selected because they performed well with the small-to-medium size datasets that were used for this work, and are robust to moderate non-deterministic noise, typical from experimental acoustic signals. This was shown to be the case for our datasets.

To explain the basis of HGBR, we first outline the basic idea behind simple Gradient Boosting regression. The core concept is that the model improves iteratively based on the gradients of the loss function computed from the previous iteration. Specifically, given true (usually observed) output data $\mathbf{y}$ and an input matrix $\mathbf{X}$ whose columns are potential predictors of $\mathbf{y}$, the model computes an estimate $\hat{\mathbf{y}}$ through an iterative procedure

$$\hat{\mathbf{y}} = F_M(\mathbf{X}) = \sum_{m=1}^{M} \gamma_m h_m(\mathbf{X}) \tag{6}$$

where M is the number of boosting iterations, h_m represents the weak learner at iteration m, which integrates the improvement derived from the previous iteration, and γ_m is the corresponding learning step. The overall objective is to minimize a loss function, defined as:

$$\mathrm{L}(\mathbf{y}, \hat{\mathbf{y}}) = \frac{1}{n}\sum_{i=1}^{n}(y_i - \hat{y}_i)^2 \tag{7}$$

where n denotes the total number of data points, which in this context corresponds to the length of the time series.

This expression usually defines the general structure of the different gradient boosting models. However, it is often more informative to describe the iterative procedure explicitly. At the first iteration, a constant model γ is assumed:

$$F_0(\mathbf{X}) = \arg\min_{\gamma} \sum_{i=1}^{n} \mathrm{L}(y_i, \gamma) \tag{8}$$

which means that the first step is concerned with finding the optimal constant that best approximates the target variable. For iterations

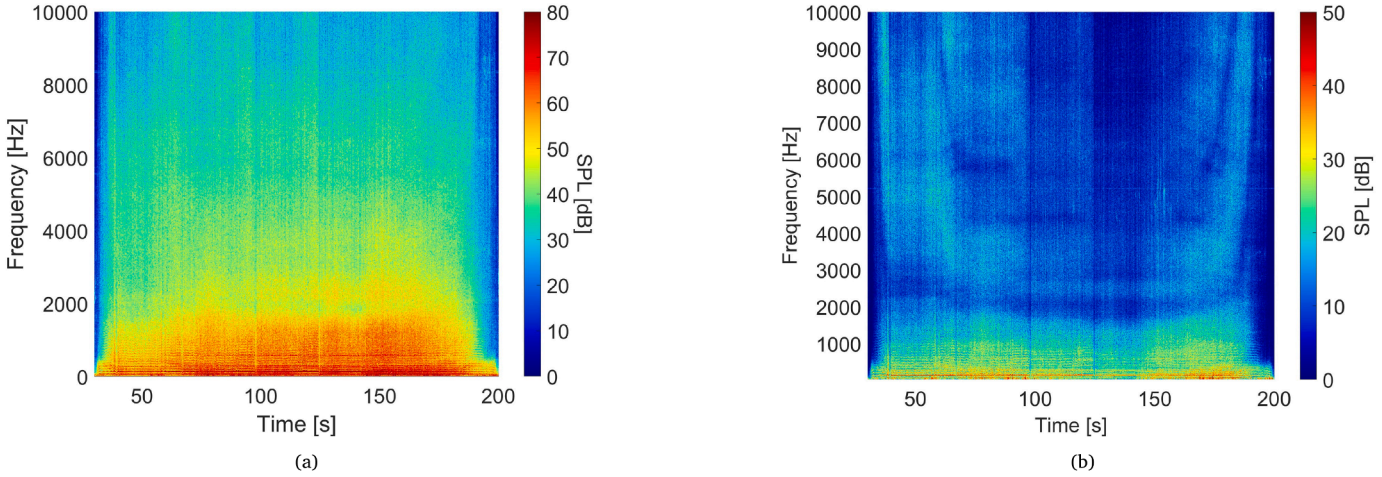


Fig. 3. Beamformed Fig. 3a and single-microphone Fig. 3b spectrograms. The beamformed spectrogram is backpropagated to the 1 m hemisphere around the drone, while the single microphone spectrogram reflects the acoustic dynamics at the array position, hence the difference in dB levels between both.

$m = 1, \ldots, M$, pseudo-residuals $r_i^{(m)}$ are computed as follows:

$$r_i^{(m)} = -\left[\frac{\partial \mathrm{L}(y_i, \hat{y}_i)}{\partial \hat{y}_i}\right]_{\hat{y}_i = F_{m-1}(\mathbf{X}_i)} \tag{9}$$

which makes it explicit that the update is driven by the gradient of the loss function. This equation considerably simplifies if the loss is the squared error: $r_i^{(m)} = y_i - F_{m-1}(\mathbf{X}_i)$.

Next, a learner $h_m(\mathbf{X})$ is fitted to the residuals $r_i^{(m)}$. This learner is a decision tree with K leaves, which partitions the input space into K regions $R_1, \ldots, R_K$. Within each region, the tree prediction is constant, so we have: $h_m(\mathbf{X}) = \sum_{k=1}^{K} \eta_{mk} \mathbf{1}_{\{\mathbf{X} \in R_k\}}$, with η_{mk} being the predicted value at leaf k in iteration m. For squared error loss, we choose η_{mk} to minimize the loss over the sample in that leaf:

$$\eta_{mk} = \frac{1}{N_k} \sum_{\{i: \mathbf{X}_i \in R_k\}} r_i^{(m)} \tag{10}$$

where N_k is the number of samples in region R_k, which means that η_{mk} is the mean of residuals in leaf k. Mathematically, the learner fits each leaf by taking the mean of the residuals in that region. The model is then updated as:

$$F_m(\mathbf{X}_i) = F_{m-1}(\mathbf{X}_i) + \gamma h_m(\mathbf{X}_i) \tag{11}$$

where γ is the learning rate. The procedure described between Eqs. (9) and (11) is repeated until M boosting iterations are completed.

So far, the method corresponds to the standard gradient boosting regression trees method. In these conventional methods, once the regions R_k are defined, the learner output follows the classic operation of decision trees, where all possible split thresholds are evaluated to find the one that minimizes the prediction error. The histogram-based approximation consists of simplifying this splitting evaluation, increasing the speed of the algorithm. In HGBR, a quantization of each input variable is defined by calculating quantile-based or uniform bins. Instead of searching over all continuous values for the best split threshold, the algorithm considers only splits at the bin boundaries. This procedure reduces the computational complexity of the algorithm and significantly accelerates training without major loss of predictive performance.

3. Results

In Section 3.1, we describe the dynamics of different studied acoustic metrics. Section 3.2 details the derivation of the telemetry-based variables. Once the full set of initial inputs is defined, Section 3.3 describes the development, assumptions, and results of the models for both OSPL and OASPL.

3.1. Acoustic metrics

Using the beamforming and backpropagation methods described in Section 2, the acoustic data from each operation were transformed into spectrograms with improved signal-to-noise ratio. This leads to considerably reduced influences of ground reflections, and hence to spectrograms that are more descriptive of the acoustic far fields on the 1 m hemisphere around the drone. The spectrogram of one operation is illustrated in Fig. 3.

As a first step in developing the models for predicting the sound from the drone operations, two simple metrics are considered: OSPL and OASPL, i.e., the unweighted and A-weighted overall sound pressure level. Fig. 4 presents the OSPL and OASPL values back-propagated to the source for one of the operations described in Section 2.1.

A tone reconstruction algorithm was developed to assess the intensity and contributions of the tonal component to the OSPL and OASPL. Using this, we found that tones were present up to 800 Hz, above which the broadband intensity becomes dominant and tones are no longer identifiable.

3.2. Telemetry-based input parameters

As it is not known a-priori which operational parameters are needed to predict the OSPL or OASPL, we first calculate a broad range of telemetry-based observables. We focus on variables whose dynamics reflect, either directly or indirectly, changes in the UAV's state of motion. The assumption is that any OSPL or OASPL variation corresponds to a telemetry quantity showing a consistent change. In this sense, we investigate variables indicative of changes in drone position and velocity, such as translational displacements and attitude variations in a multirotor system.

Some variables are derived purely from the instantaneous drone propellers' rotational speeds (RPM), while others, such as the drone's speed vector, are not. These variables, although a consequence of specific RPM profiles, are also dependent on the drone dynamics. As it is unclear which type better predicts sound variations, both categories are included in the initial input variables set.

3.2.1. Observables related to translational motion

We first derive RPM-based observables associated with translational motion, indicated by the arrows in Fig. 5. These arrows represent the main translation motion, though small planar movements may also occur during the operation.

Translational movement arises when all the upper rotors operate at the same rotational speed, and all the lower rotors operate at the same,

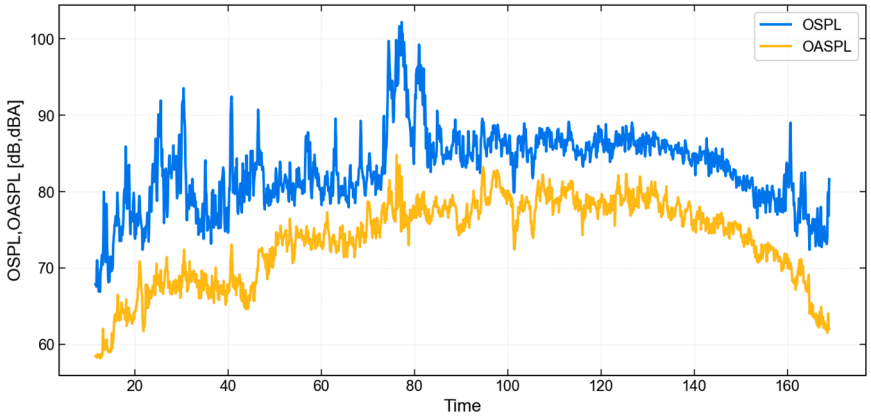


Fig. 4. Comparison of beamformed OSPL and OASPL signals from a UAV Gorgon operation.

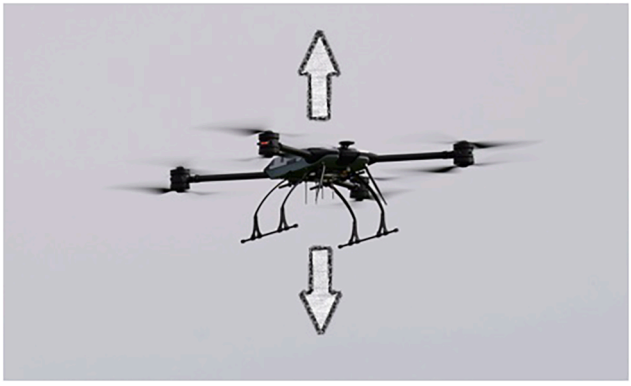


Fig. 5. Sketch indicating the type of displacements. The arrows show the main translations corresponding to the performed maneuvers. Small horizontal displacements may also occur and is examined separately when analyzing observables corresponding to UAV attitude variations.

but different from the upper one. Therefore, we consider, as input variables, the average rotational speeds of the upper set $n_r^{(U)}(t)$ and lower set $n_r^{(L)}(t)$ as follows:

$$n_r^{(U)}(t) = \frac{1}{N^{(U)}} \sum_{i=1}^{4} n_{r,i}^{(U)}(t) \tag{12}$$

and

$$n_r^{(L)}(t) = \frac{1}{N^{(L)}} \sum_{i=1}^{4} n_{r,i}^{(L)}(t) \tag{13}$$

where $n_{r,i}^{(U)}(t)$ and $n_{r,i}^{(L)}(t)$ are the RPM activity of the i^{th}, $i = 1, \dots, 4$ rotor from the upper and lower set respectively.

We observed that during ascend, hover, and descent, the upper and lower rotors operated at different RPMs. In some operations, the entire $n_r^{(U)}$ and $n_r^{(L)}$ signals were different, while in other operations, differences appeared only in specific time intervals. Fig. 6(a) and (b) illustrate the Mach tip numbers for the upper and lower sets, along with their standard deviations. Two typical operations are shown: one where the signals differ throughout the operation, and the other where the differences occur only during some maneuvers.

As shown in Fig. 6(a) and (b) , both $n_r^{(U)}$ and $n_r^{(L)}$, represented here as their Mach tip numbers $M_T^{(U)}$ and $M_T^{(L)}$, exhibit a sharp increase in activity at the onset of each ascent stage, which break the stationary hover dynamics. After this initial surge, the rotors activity decreases as it ascends at an approximately constant speed, and is then significantly reduced when reaching the hover altitude. As this reduction can overshoot the required hover thrust, a slight increase in rotor activity is observed immediately afterward. This pattern is repeated at each ascent-hover cycle. Then, during descent, most of the differences between both sets of rotors appear and no specific pattern was identified. The overall higher activity from the lower sets could be due to the increased inflow velocity on the downstream propellers, which effectively would cause a reduction of thrust if the angular speed of the downstream propeller is not increased.

To account for outdoor operation, where trajectory perturbations are expected, we also include the standard deviations of both upper and lower rotor speeds: $\sigma(n_r^{(U)})(t)$ and $\sigma(n_r^{(L)})(t)$. They indicate how much individual rotor activity within each set deviates from the mean values $n_r^{(U)}(t)$ and $n_r^{(L)}(t)$. Including these deviations allows the model to capture potential variations of the drone attitude.

Also quantities directly describing translational variations should be considered. Therefore, vertical acceleration and velocity, a_z and v_z, were included in the initial variable set, along with thrust and mean advance ratios. This is further motivated by findings from previous studies described in Section 1. The advance ratios describe the efficiency of the upper and lower rotational speeds in producing a given velocity. These were calculated as:

$$J^{(U,L)} = \frac{v}{n_r^{(U,L)} D} \tag{14}$$

where $n_r^{(U,L)}$ are the mean rotational speeds in cycles per second of the upper or lower set of rotors, respectively, v is the UAV velocity in m/s, and D is the propeller diameter in m.

The advance ratios during the fourth and fifth operations can be observed in Fig. 6(c) and (d). These specific quantities describe how efficient the upper or lower set of rotors are if individualized from the CRP dynamics; inflow and swirl-induced modifications are not taken into account when describing the velocity in the lower advanced ratio $J^{(L)}$. As mentioned however, the increased lower Mach tip number during ascent or hover is likely reflecting the presence of a reduction of angle of attack caused by the induced flow velocities from the upstream propellers into the downstream ones.

As it was observed that $\sigma(n_r^{(U)})(t)$ and $\sigma(n_r^{(L)})(t)$ are nonzero and potentially important, they also generate corresponding variations in the advance ratios. Therefore, these effects are considered by propagating $\sigma(n_r^{(U)})(t)$ and $\sigma(n_r^{(L)})(t)$ into $\sigma(J^{(U)})(t)$ and $\sigma(J^{(L)})(t)$. Because these deviations represent variations among rotors at equal times, such equivalent quantity does not exist for the speed. Therefore, the propagation only accounts for time-like variations in the rotational speeds. Including the deviation from the means $J^{(U,L)}$ allows the input set to have a representation of nonlinear effects at the advanced ratio level. The $\sigma(J^{(U,L)})$ signals during the fourth and fifth operations can be observed in Fig. 6(c)

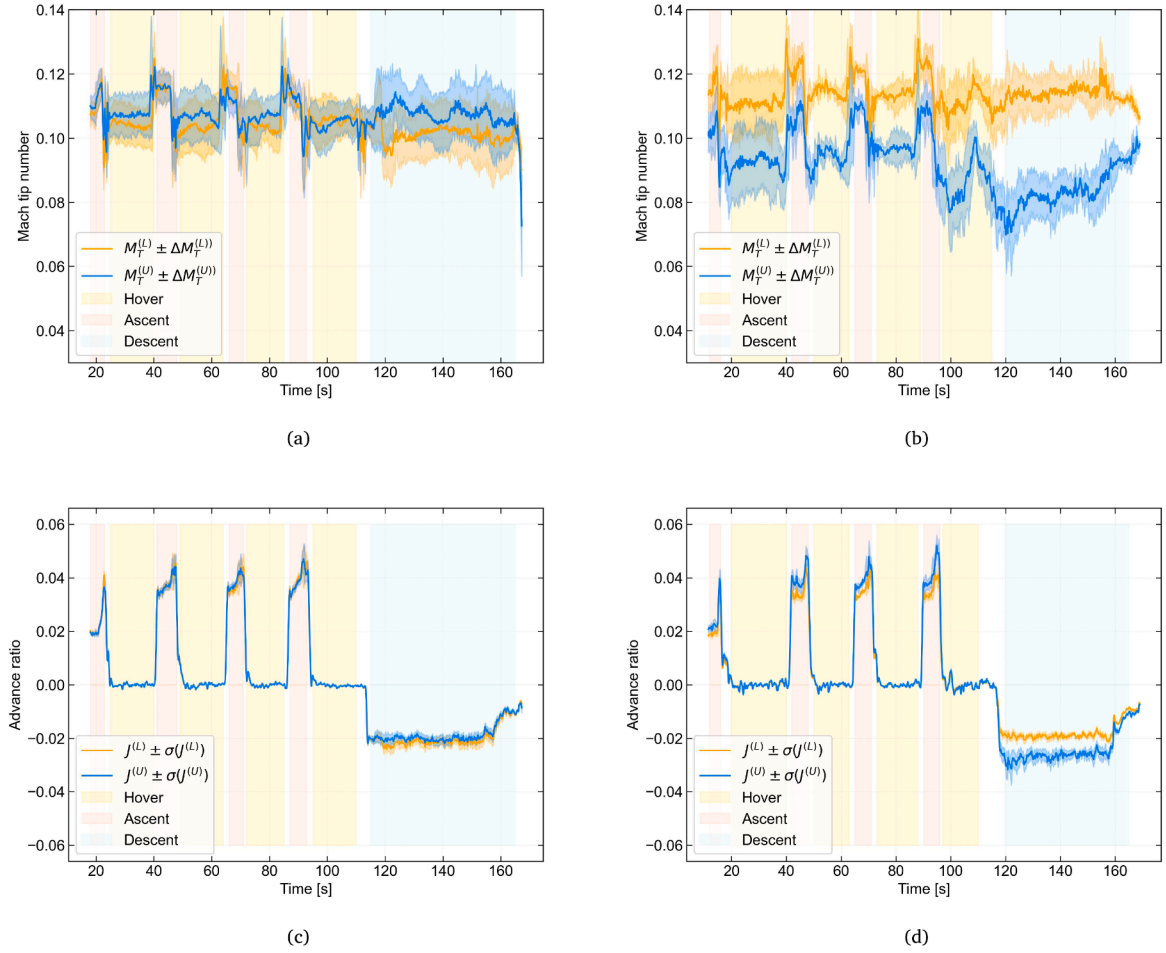


Fig. 6. (a) and (b): Mach tip numbers of the 4th and 5th operation. (c) and (d): advance ratios of the 4th and 5th operation.

and (d), and are calculated through:

$$\sigma(J^{(U,L)})(t) = \frac{v}{D} \frac{\sigma(n_r^{(U,L)})(t)}{(n_r^{(U,L)})^2} \tag{15}$$

The thrust signal during the fourth operation can be observed in Fig. 7. The behavior described for the $n_r^{(U)}(t)$, $n_r^{(L)}(t)$ becomes clearly evident in the thrust, where at the onset of each ascent stage, a high-amplitude and sharp thrust peak occurs over a short time scale. The thrust is then reduced to accomplish a constant ascent rate. Consistently, as seen in Fig. 6(c) and (d), the effective advance ratios of the upper and lower sets become non-zero during the ascent and descent stages, with some small fluctuations occurring during the hover instances. The repetitive pattern observed in Fig. 6 happens during the second and third ascents in this operation, and less clearly during the fourth ascent, where clear thrust oscillations appear. This could be due to pilot's action or environmental factors. A different thrust profile is observed in the first ascent, as the take-off had just taken place (the take-off and subsequent instances are not shown in the figure).

3.2.2. Attitude variations observables

In the previous section, the variables introduced reflected translational movement changes, and certain attitude variations caused by mismatches in the rotational speeds among rotors within the same upper or lower set. We now build additional variables to reflect other types of attitude variations that occur when the thrust from a pair of CRPs of a given arm differ from pairs at other arms. This behavior can result from wind perturbations, drone control system compensation, or pilot input, leading to variations in the pitch and/or roll of the drone.

To capture these effects, the mean activity of each CRP pair at each arm was calculated, resulting in four different signals $\bar{n}_r^{A_i}(t)$. Because the goal is not to identify which perturbation corresponds to which arm, we reduced the dimensionality by taking the mean value of these signals:

$$n_r^{(A)}(t) = \frac{1}{N^{(A)}} \sum_{i=1}^{4} \bar{n}_r^{A_i}(t) \qquad \bar{n}_r^{A_i}(t) = \frac{(n_r^{(U,A_i)}(t) + n_r^{(L,A_i)}(t))}{2} \tag{16}$$

where $n_r^{(A)}$ is the average RPM over all four drone arms, and $\bar{n}_r^{A_i}$ is the average RPM for arm A_i, calculated as the mean between the upper and lower RPMs on that arm.

This quantity can be used to describe the fast variations mentioned earlier, as deviation from $n_r^{(A)}$ indicates the degree at which any CRP rotated at a different speed than the rest. Specifically:

$$\sigma(n_r^{(A)})(t) = \frac{1}{\sqrt{4-1}} \sqrt{\sum_{i=1}^{4} (\bar{n}_r^{A_i}(t) - n_r^{(A)}(t))^2} \tag{17}$$

Similarly as observed in Figs. 6 and 7, $M_T^{(A)}$ shows a repetitive pattern of increase and decrease when an ascent starts and ends, and a stabilization during hover. However, differences are observed in the relative amplitude and timing of sharp events around the onset of an ascent or stabilization, which reflects the independent behavior of this metric relative to the ones presented so far.

Finally, to have a metric of how differently the activity of the rotors from a CRP pair behaves in time, the mean of the differences $\Delta n_r^{(A)}$ is

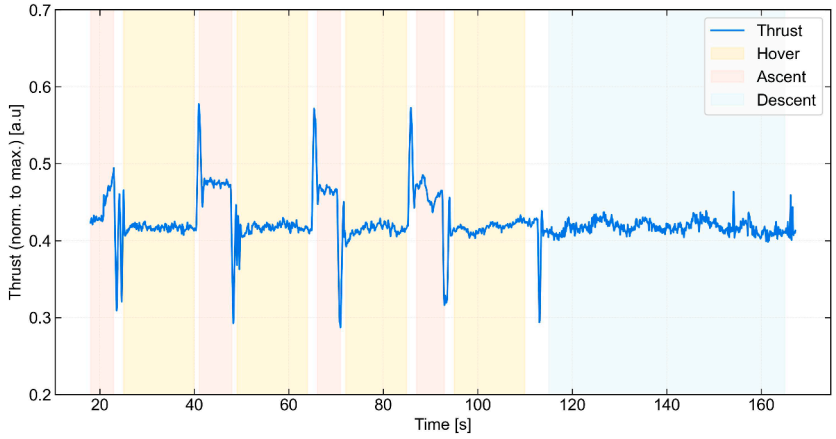


Fig. 7. Normalized thrust during the fourth operation.

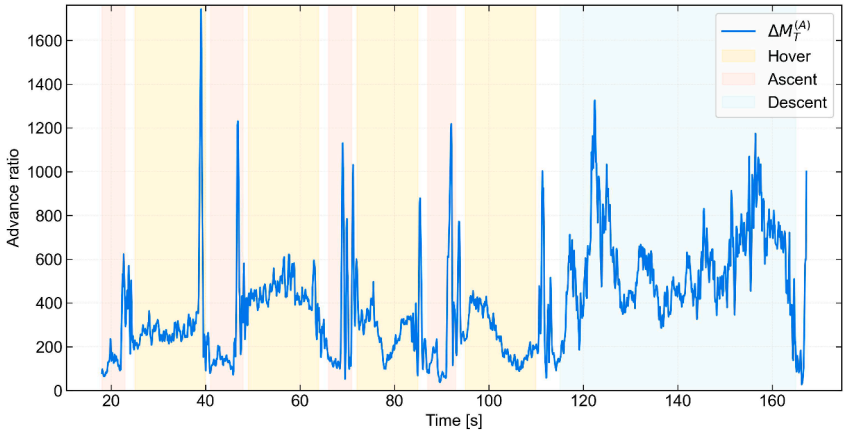


Fig. 8. Signal $\Delta(M_T^{(A)})$ during the fourth operation. Although the repetitive patterns are evident, this observable reflects different perturbations within a manouevre, which was not as clearly observed in Figs. 6, 7.

computed as:

$$\Delta n_r^{(A)}(t) = \frac{1}{N^{(A)}} \sum_{i=1}^{4} \Delta n_r^{A_i}(t) \qquad \Delta n_r^{A_i}(t) = \frac{|(n_r^{(U,A_i)}(t) - n_r^{(L,A_i)}(t))|}{2} \tag{18}$$

The equivalent difference in Mach tip number $\Delta(M_T^{(A)})$ during the fourth operation is shown in Fig. 8. Its dynamic is qualitatively different from that of $M_T^{(A)}$, as it reflects the mean-over-arms difference between the upper and lower rotors, which is not reflective of the net thrust.

Additionally, to have a direct representation of the drone attitude variations, the absolute value of the angular speeds $\dot{\psi}$ was included as well.

As shown in all telemetry figures, all input variables are expressed as dimensionless quantities to ensure unit-consistent relations when developing the models. Therefore, for purely rotors' rotational speed-based quantities, the corresponding Mach tip numbers are considered. For velocity, the vertical Mach number M_z is considered, whereas acceleration a_z and thrust T are normalized to their maximum values. Therefore, in general:

Variable	Dimensionless equivalent
$n_r^{(U,L)}$, $\sigma(n_r^{(U,L)})$, $n_r^{(A)}$, $\sigma(n_r^{(A)})$, $\Delta n_r^{(A)}$	$M_T^{(U,L)}$, $\sigma(M_T^{(U,L)})$, $M_T^{(A)}$, $\sigma(M_T^{(A)})$, $\Delta M_T^{(A)}$
T, v_z, a_z	$T^{(n)}$, M_z, $a_z^{(n)}$

3.2.3. *Timescales considerations*

So far, the selection of candidate inputs has focused on the flight dynamics telemetry. However, as observed in Fig. 4, the dynamics of OSPL and OASPL are likely also affected by the emission angle, and therefore by the radiation pattern. We hypothesize that the radiation pattern results in a modulation of the signal trend, whose period is unknown. At the same time, telemetry observables also exhibit behaviors over different timescales: rapid variations over a few time instances, and slower variations over intermediate times in the order of seconds, as illustrated for thrust in Fig. 7. In this example, extreme thrust bursts occur when the drone begins and finishes each intermediate ascend stage, while slower thrust patterns appear over a few seconds during hover and ascent.

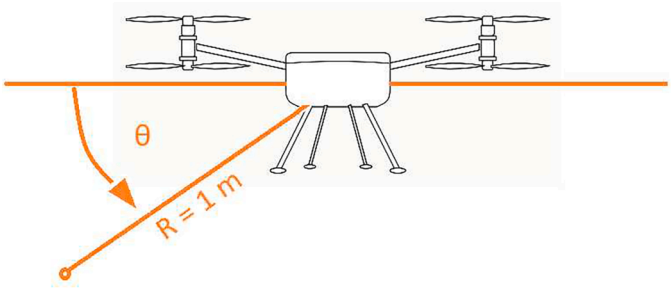
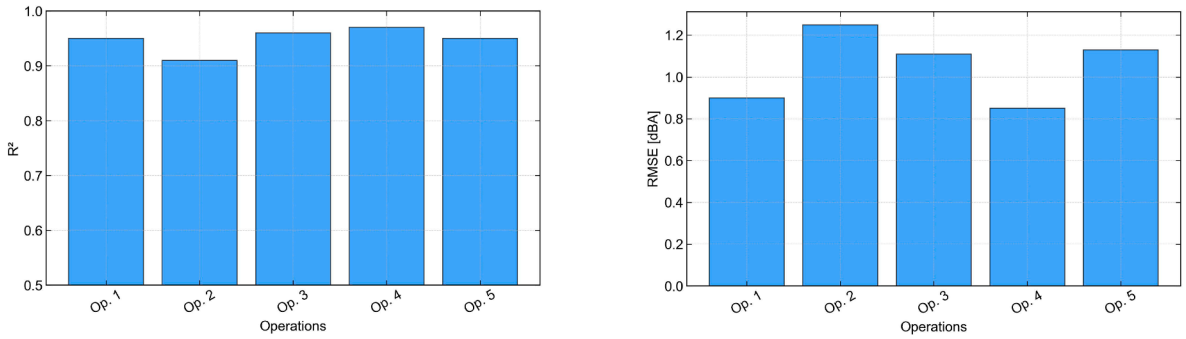


Fig. 9. Sketch displaying the elevation angle θ. The angle is measured as the angle between the ground and the drone position vector. As vertically opposite angles are always equal, the same angle is defined between the horizontal plane of the drone and the sample point on the one-meter hemisphere, as shown in the sketch.



(a) R^2 from $OASPL$ prediction per operation.

(b) $RMSE$ from $OASPL$ prediction per operation.

Fig. 10. OASPL model performance results using the full set of coupled variables. The accuracy of each model is above 85%, with RMSE values up to 1.3 dBA. This quality is a necessary condition to ensure that the search for key telemetry-based variables is meaningful, and that they are correctly identified.

Because these coupled timescales behaviors are generally unknown, the entire signal is modeled while considering the effect of the emission angle. A graphical description of this angle can be observed in Fig. 9.

To keep this dependence simple, few requirements are imposed on the modulation function: it should approach zero as $\theta \to 0$, to represent the observed dipolar behavior, and remain nonzero for other angles up to 80 degrees (the highest tested angle). The simplest function fulfilling this condition is $\sin(\theta)$. Then, to capture this coupling over several timescales, we model the interaction as $x_i \sin(\theta)$, where x_i is each telemetry-based variable. All x_i are normalized to 1 to ensure comparable magnitudes. The azimuthal angle is not taken into account as the studied maneuvers were performed at different but fixed values of ϕ. Therefore, the complete set of potentially important input variables is:

$$\{T, M_z, J^{(U)}, J^{(L)}, M_T^{(U)}, M_T^{(L)}, \sigma(M_T^{(U)}), \sigma(M_T^{(L)}), \sigma(J^{(U)}), \sigma(J^{(L)}), a_z, \sigma(M_T^{(A)}), \Delta M_T^{(A)}\} \tag{19}$$

where the $\sin\theta$ term multiplying each variable is omitted for visual clarity, as well as the n superscript in T and a_z.

As observed, this leads to a large number of input variables. However, this set is not intended to present a definite group of variables; it serves only as a first step to study the importance of each variable and selecting predictors within this group. Additionally, we do not require all variables to be physically independent as it is unclear whether the acoustic performance, expressed as OSPL and OASPL, can be "regressed" from more fundamental variables such as RPM-based, or effective variables like thrust. Finally, since all telemetry data streams had a higher sampling rate than the beamformed acoustic data, the input signals were time-averaged to match the window size of 0.1 s for both OSPL and OASPL.

3.3. Model predictions

Assuming that deterministic events in OSPL and OASPL result from changes in the telemetry variables at a given time, the data from each operation were randomized and split into 70% training-validation and 30% test datasets. The testing dataset is kept aside and never used during training, validation or optimization. For each operation, an extensive grid search was first performed to optimize the model hyperparameters on the validation set. For each tested combination, the HGBR model is trained on 75% of the training-validation data, and predictions were compared with the corresponding validation outputs. This process was repeated several times with different training and validation subsets, varying the maximum number of iterations, maximum depth of decision trees, minimum samples per leaf, learning rate, and maximum bins. Then, the optimal combination of hyperparameters is the one that maximizes R^2. The same hyperparameter search space was considered in both OSPL and OASPL, as summarized in Table 2.

Table 2
Different combinations of hyperparameter values tested during HGBR model optimization for best performance.

Maximum iteration	50, 100, 200, 500, 700, 1000, 1200
Maximum tree depth	5, 10, 15, 20, 30
Minimum sample number per leaf	1,2,4,5,10,20, 50, 100
Learning rate	0.01, 0.05, 0.1, 0.2,0.3
Maximum number of bins	255, 300, 500, 700

After completing the optimization, the testing phase is conducted. The trained model, with fixed parameters, is applied to the testing dataset inputs to generate predictions. The predicted values are then compared with the corresponding acoustic outputs, and subsequently the R^2 and $RMSE$ are calculated to investigate the model accuracy and precision on unseen data.

Because variability is expected a-priori across similar conditions in different operations, we allow the telemetry variables to vary accordingly, e.g. reflecting the variability of real flight environments. Therefore, the models were firstly optimized and tested on each operation separately. For example, the variations may arise from wind gusts or pilot actions, both of which can perturb the drone flight dynamics away

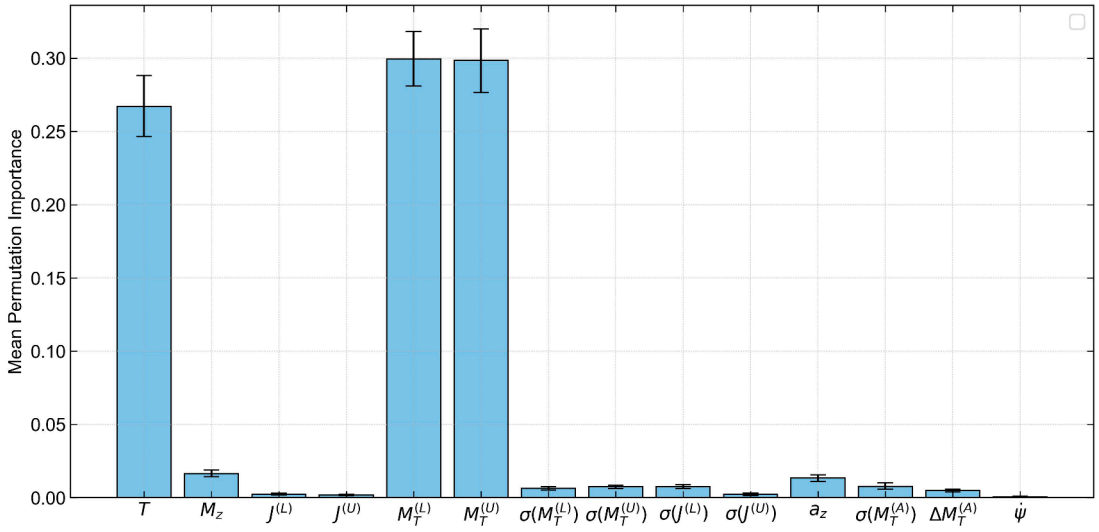
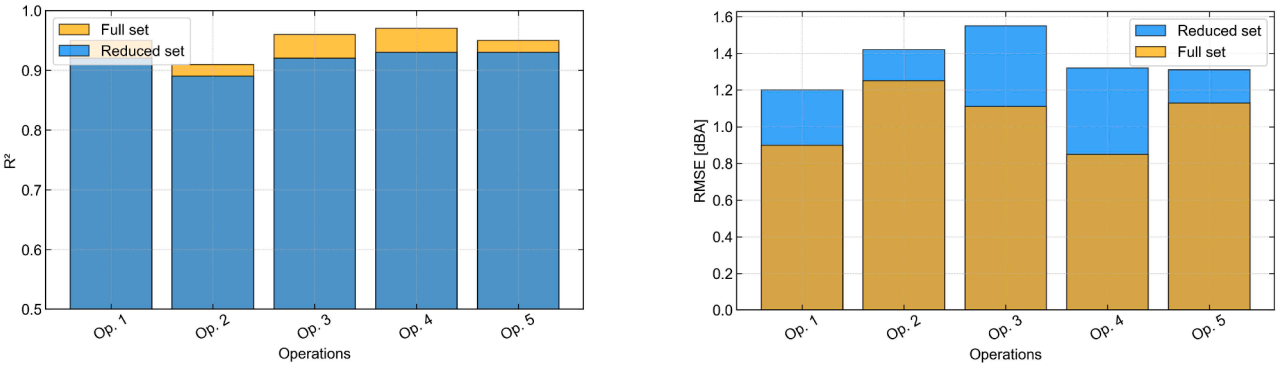


Fig. 11. Confidence intervals for each variable from the $OASPL$ predictions across all operations obtained from the bootstrapping method. As can be observed, the three dominant variables are $M_T^{(L)}\sin(\theta)$, $M_T^{(U)}\sin(\theta)$, $T\sin(\theta)$. This was determined on the mean values as well as in the upper bounds of each interval. The multiplicative $\sin(\theta)$ was not included in the label names for visual clarity.



(a) R^2 per operation

(b) $RMSE$ per operation

Fig. 12. Model performance comparison between reduced and full variable sets across all operations. As expected, the R^2 gets reduced, and RMSE increases compared to the model with the full variables. However, R^2's are above 0.89 and the RMSEs under 1.60 dBA, reflecting a good prediction capability.

from a stable trajectory. By analyzing each operation separately, we may identify operation-specific influential variables. When the model is later generalized across all operations, it helps understand which of these guide most of the acoustic dynamics.

3.3.1. HGBR model of OASPL dynamics

HGBR models were trained to predict OASPL and OSPL of each operation separately using the full set of telemetry variables coupled to the $\sin(\theta)$ (coupled variables). The testing results, in terms of R^2 and RMSE per operation, are illustrated in Fig. 10.

As shown, the model performs accurately and consistently across all operations, accomplishing R^2 values above 0.90 in all cases, with a mean of 0.92 across operations, and mean $RMSE$ value 1.04 dBA.

To gain a deeper understanding of the noise dynamics and generate a meaningful predictive model, it is important to identify key variables driving the observed OASPL dynamics. For this purpose, the *permutation importance* of each variable was calculated. This metric quantifies the decrease in model performance when the original variables are randomly shuffled and replaced into the trained model. A higher value indicates a greater reduction on prediction accuracy, thereby indicating higher importance of the specific variable. The detailed definition of this importance is provided in the Supplementary material section.

To identify common variables across all operations, we argue these should correspond to acoustic effects consistently observed across most datasets. In other words, most of the deterministic time-dependent acoustic features should be observed across all operations. To find variables that can significantly guide the predictions of these shared effects, the variable importance scores from each operation were combined in a way that accounts for and propagates variability among operations.

The relevance of these variables in generating accurate predictions across all operations can then be tested: if key variables are identified, they should be able to accurately predict the experimental data in each operation. In contrast, if the prediction fails for an operation or time interval, it implies that some deterministic effect was not captured by the assessment of the combined operations.

To compute the variable importance, the permutation importance from each operation was considered [28], and *bootstrapping* was used to estimate the confidence interval for each variable over all operations. The details of the statistical method are provided in the supplementary material. The 95% confidence intervals (CI) were calculated between the (2.5% – 97.5%) percentiles. The final set of important variables was defined such that re-training and re-testing a model using only these variables lead to $R^2 \geq 0.85$ for all operations. This threshold was chosen to be approximately the same as the minimum accuracy obtained using the full set. It was found that including the four most important variables

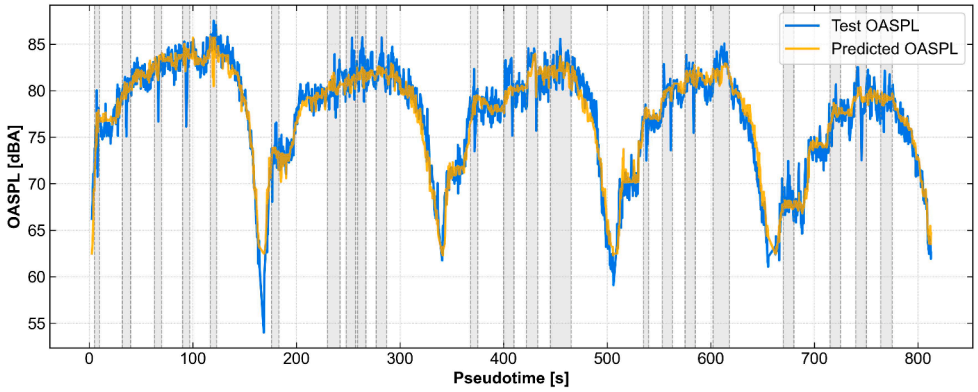
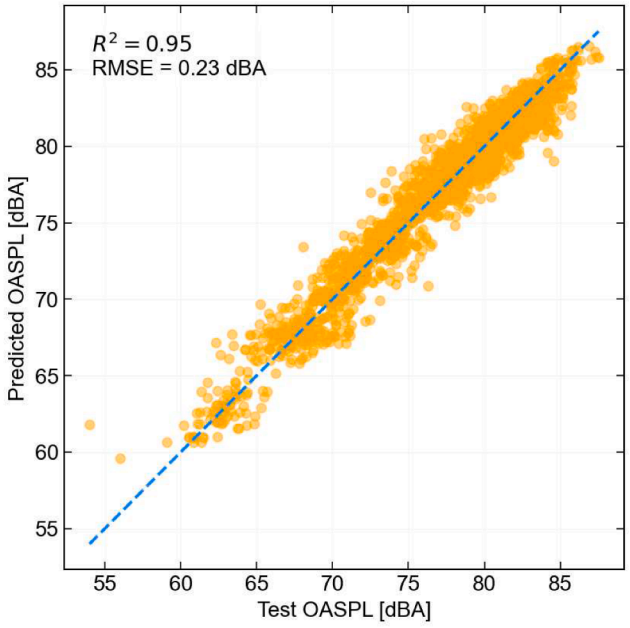
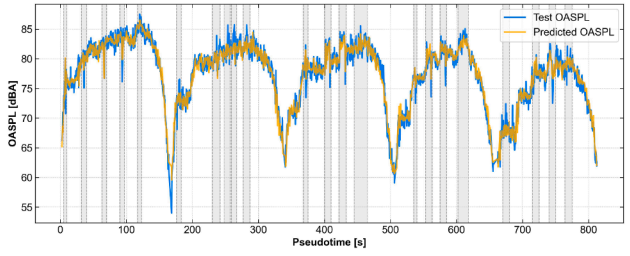


Fig. 13. Observed (true) and predicted OASPL using only $M_T^{(U)}\sin(\theta)$ and $M_T^{(L)}\sin(\theta)$ as a function of time. This test set represents 30% of unseen data. Light gray areas show instances where short- and mid-timescale behaviors are not captured. The trend and some faster variations are well predicted, which is sufficient to provide adequate R^2 and RMSE values. However, the model misses parts of faster dynamics, that include sharp peaks and deep valleys, as well as intermediate trends.



(a) Scatter plot of the predicted $OASPL$ as a function of the true $OASPL$ corresponding to the test data.



(b) Plots of the predicted and test OASPLs as a function of pseudotime. The horizontal axis has units of time, but the operations were not performed one immediately after the other.

Fig. 14. Predicted $OASPL$ from the single HGBR model of the combined operations using the input variables $M_T^{(U)}\sin(\theta)$, $M_T^{(L)}\sin(\theta)$, $T\sin(\theta)$, and $M_z\sin(\theta)$. The true data displayed in both figures corresponds to the 30% unseen test data. The model manages to accurately predict most time-dependent features of the $OASPL$ across all operations, accomplishing a $R^2 = 0.95$ and RMSE = 0.23 dBA. The long- and mid-timescale behaviors are well predicted. A larger number of fast events is also captured. The events shown in light gray corresponded to those that were not be fully captured in Fig. 13, but are now better predicted.

met this accuracy requirement. The results of this analysis are illustrated in Fig. 11.

This study shows that, to capture the main dynamics of $OASPL$ in each operation, the key variables should contain some of the first most important parameters: $M_T^{(L)}\sin(\theta)$, $M_T^{(U)}\sin(\theta)$, $T\sin(\theta)$.

The final set of key variables was defined such that re-training and re-testing a model using only these variables leads to $R^2 \geq 0.85$ for all operations. This threshold was chosen to be approximately the same as the minimum accuracy obtained using the full set. This condition was met by including only $M_T^{(L)}\sin(\theta)$ and $M_T^{(U)}\sin(\theta)$. The resulting R^2 and RMSE, comparing the full and reduced variable sets, are illustrated in Fig. 12.

As can be seen, re-training and re-testing the HGBR models using only $M_T^{(U)}\sin(\theta)$ and $M_T^{(L)}\sin(\theta)$ leads to all R^2 values above 0.89, with an average value of 0.92. The RMSEs are below 1.60 dBA, with a mean value of 1.36 dBA. The high quality of the predictions can be explained by the nature of the $A-$weighting, which reduces the low-frequency contributions, hence attenuating any amplitude fluctuations from the tonal component.

OASPL can be represented by its general trend, which is well captured by the sine of the emission angle. However, $\sin(\theta)$ alone cannot achieve consistent performance across operations, and therefore its coupling with $M_T^{(U)}$ and $M_T^{(L)}$ is needed to predict most short- and middle-timescale behaviors. Using only $\sin(\theta)$ as input, the average R^2 drops to 0.84. The lack of consistent prediction in shorter timescales implies that, while the trend is a good predictor for some operations, the $\sin(\theta)$ alone is insufficient to explain variations in measured OASPL beyond the trend: The accuracy for the first operation even falls to 0.70, below the required threshold. This is not the case when using $M_T^{(U)}\sin(\theta)$ and $M_T^{(L)}\sin(\theta)$, see Fig. 12.

These results indicate that good R^2 and RMSE values are mainly reflecting accurate trend prediction. Only relying on these metrics can be misleading, because the short- and middle-timescale behaviors may still be poorly predicted. Therefore, while high R^2 and low RMSE are necessary conditions to assess the prediction performance, they are not sufficient. Visual examination of the predicted time series is thus essential. Such inspection can help evaluate whether deterministic fast behaviors are captured. After visual verification, the prediction improvement achieved by reducing the input set can be quantified using differences in R^2 and RMSE, rather than absolute values.

The generalization capacity of the model and predictors was studied using the combined dataset of all operations. The initial predictors were $M_T^{(U)}\sin(\theta)$ and $M_T^{(L)}\sin(\theta)$. As before, 70% of the data was utilized for training and optimization, and 30% was used for testing. Fig. 13 illustrates the predicted and testing OASPL signals of all operations. The overall trend is properly captured. However, fast and large-amplitude

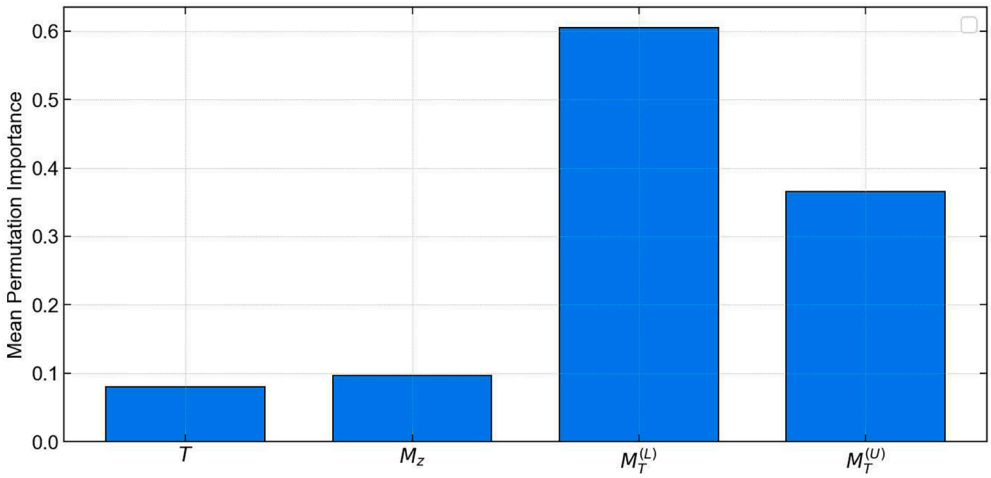
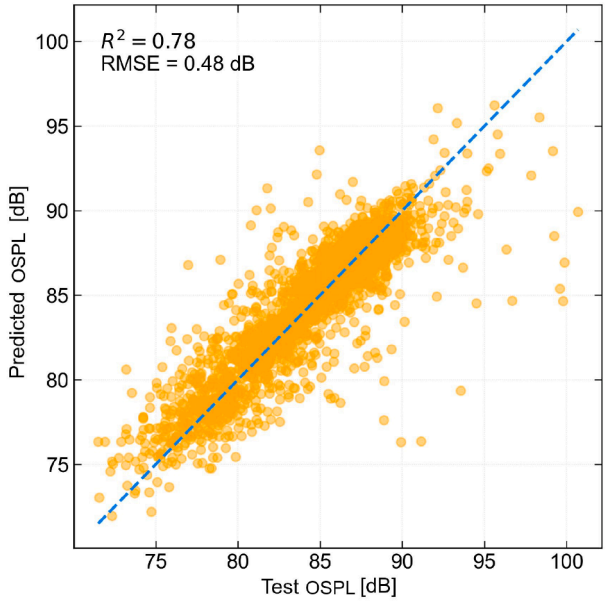
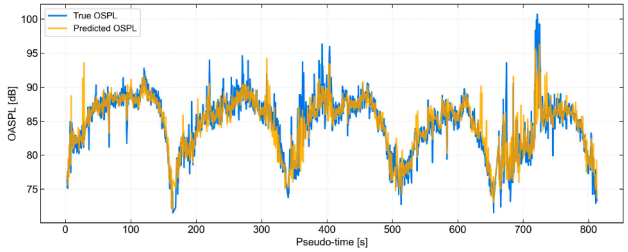


Fig. 15. Variable importance of the OASPL model for the combined operations dataset.



(a) Scatter plot of predicted $OSPL$ versus measured $OSPL$ on the testing (unseen) data.



(b) Predicted and measured OSPL as a function of pseudo-time. The horizontal axis has units of time, but operations were artificially plotted consecutively.

Fig. 16. Predicted $OSPL$ from the single HGBR model combining all operations and using only the selected variables. The true (measured) data in both frames corresponds to the 30% unseen test data from all operations. The model captures most of the time-dependent features of $OSPL$ across all flights, accomplishing $R^2 = 0.78$ and RMSE = 0.48 dB.

fluctuations, as well as some mid-timescale dynamics cannot be represented.

As observed in Fig. 13, certain short-timescale events appear across all operations with large-enough values to suggest they are not stochastic noise. Out of these, the events that are not captured by the model were visually identified.

For some of the low level peaks, their occurences coincide with the ascend intervals between hovers, or between consecutive ascents. This implies that a possible cause for these behaviors is a quantity related to the UAV's acceleration or thrust. Hence, the thrust was included in the input set to determine whether it explains this effect. On the other hand, other fast events not captured by the initial model showed different temporal behavior. They occur over longer periods rather than fast bursts, and involve increases in sound level lasting around 5 to 15 s. These coincide with the full hovers or full ascent phases, possibly indicating a dependency on variables with similar timescale patterns. Since the thrust did not improve the predictions of these variations, the UAV's speed was included as it has similar temporal dynamics and it appears as the next important predictor in 11. Importantly, this suggests that this variable is a possible predictor, but its adequacy must be tested by optimizing and testing the model. Considering these four variables, the combined-operation model was re-trained and re-tested. Fig. 14 illustrates the resulting OASPL predictions obtained with this final model.

As observed, several events that previously were not captured in Fig. 13 are now better predicted. The marked sharp valleys in the signal, although not fully predicted, present a clear prediction improvement over the model with only $M_T^{(U)}\sin(\theta)$ and $M_T^{(L)}\sin(\theta)$. Consistent with earlier observations, we found that thrust is primarily responsible for recovering these large fast valleys across all operations. M_z improves the predictions over the middle timescale events in OASPL. These large, sharp valleys and middle timescale behaviors are marked in gray in Figs. 13 and 14. They are particularly visible in the first, fourth and fifth operations. The effects of these added variables were assessed by re-training and re-testing the model with $M_T^{(U)}\sin(\theta)$ and $M_T^{(L)}\sin(\theta)$ as a base set, and then adding separately $M_z\sin(\theta)$ and $T\sin(\theta)$.

Most of the short-timescale peaks and valleys are partially predicted, i.e., the peak/valley timing is properly identified but the amplitude is not fully recovered. This indicates that the subset of important predictors retains consistent behavior at those time instances, which the model could effectively capture, but not predict the full amplitude.

A complete peak/valley absence, however, suggests that the predictors did not present similar short-term behavior at those times. This is likely linked to the bootstrap feature selection: some telemetry variables can likely explain those specific peaks but contribute little to the overall OASPL dynamics, and therefore were excluded from the final predictor

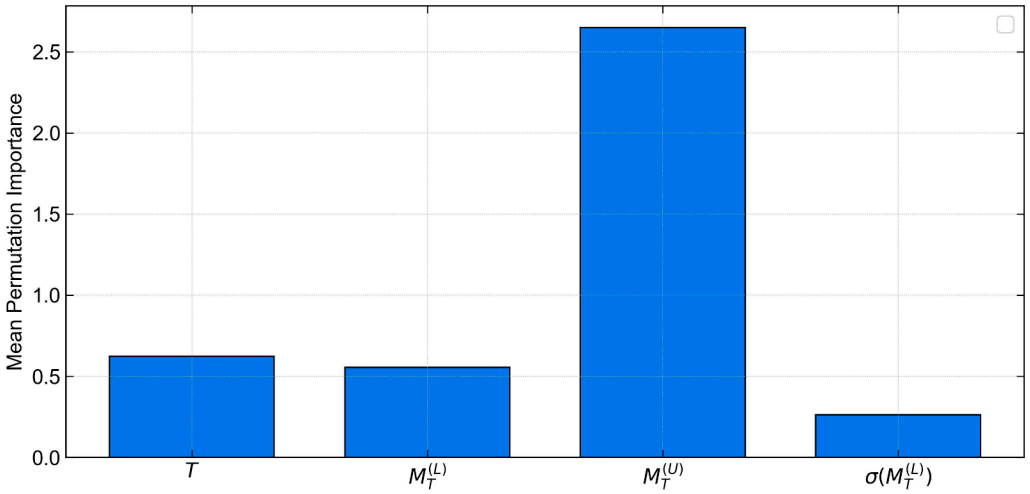


Fig. 17. Permutation importance of the HGBR model for the OSPL dynamics of all operations. As it can be seen, the variable $M_T^{(U)} \sin(\theta)$ is dominant, whereas the other variables have a similar contribution to the final predictions.

set. The complete absence of peaks could also be linked to a lack of relevant information in the initial telemetry data: either because some flight variables were not accurately recorded, or the telemetry-based descriptors are not sufficient to capture these fast fluctuations.

The resulting variable importance is shown in Fig. 15.

3.3.2. HGBR model of OSPL dynamics

Following the same model training-validation and testing methodology used for OASPL, each operation type was first studied separately using the full set of input variables. These resulted in the model performing well on unseen data, accomplishing R^2 values above 0.80 in all cases, with a mean of 0.88 across operations, and $RMSE$ values below 2 dB, with a mean of 1.36 dB.

To compute the variable importance of the combined-operations model, the permutation importance from each operation was calculated again through the confidence interval for each variable over all operations. The final set of variables was defined such that re-training and re-testing a model using only these variables lead to $R^2 \geq 0.75$ for all operations. As before, this threshold was chosen to be approximately the same as the minimum accuracy obtained using the full feature set. It was found that including the four most important variables met this accuracy requirement; $M_T^{(L)} \sin(\theta)$, $M_T^{(A)} \sin(\theta)$, $T \sin(\theta)$, and $M_T^{(U)} \sin(\theta)$.

As it was the OASPL case, reducing the input variable set did not significantly impact the model prediction performance. For $OSPL$, the largest difference between the full and reduced sets occurred in the 5th operation, with $\Delta R^2 \approx 0.05$ and the $\Delta RMSE \approx 0.25$ dB. However, the relative R^2 and $RMSE$ differences among operations remained consistent, which implies that no key variables were excluded. The small degradation in performance can likely be linked to some fast and large amplitude fluctuations in the 3rd and 5th operations that were not captured by telemetry variables.

Similarly to the OASPL case, to develop a final generalized OSPL model for all operations a single HGBR model was trained, optimized, and tested using the combined data for all operations. The predicted results and corresponding importances are illustrated in Figs. 16 and 17, respectively.

Fig. 16 shows that the generalized model captures the long-timescale behaviors of OSPL, which is linked to the coupling with the $\sin(\theta)$. This was tested by training and testing the model without including the coupling, which produced a considerable degradation of the prediction quality. It also successfully predicts most intermediate-timescale variations in all operations, where the emission angle is not the main driver. Most of the short-timescale peaks and valleys are either only partially predicted or not captured at all. This indicates that the subset of important predictors retains consistent behavior at those time instances, which the model could effectively capture, but not predict the full amplitude.

Some fast peaks and valleys are however partially predicted, showcasing that the selected telemetry-based variables can capture short-time variations, consistent with the OSPL fast behavior. This also confirms that the model can identify these patterns during the training and regenerate them during the testing. This is mostly observed in the first and fourth operations, where most peaks are correctly identified. In the fifth operation, where the largest fast peaks occur, the model still partially predicts them. However, because of their higher amplitudes, the R^2 decreases, and the RMSE increases.

To further determine which of the reduced-set variables played the significant role in this prediction, the permutation importance of this model was computed. The results are presented in Fig. 17, which shows that the dominant contribution to the OSPL prediction comes from the $M_T^{(U)} \sin(\theta)$.

4. Conclusions and discussion

Empirical models were developed to predict the OSPL and OASPL of a contra-rotating propeller UAV in real environmental conditions. OSPL and OASPL are metrics that are being largely used for legislation purposes, and therefore, they were employed as the target for the presented operational noise predictive models. These were developed from array-based acoustic data and telemetry gathered during the experimental tests in outdoor conditions. These data were converted into several meaningful variables that reflect the flight dynamics of the drone, including its perturbations caused by environmental factors such as wind gusts. From these, and using the developed models, the importance of different telemetry variables was computed, to determine which ones are critical and necessary for predicting OSPL and OASPL. The following conclusions are drawn:

- A series of new models were built, optimized, and tested on unseen data from all operations. They yielded an average accuracy of 95% for OSPL and an accuracy of 78% for OASPL, with an RMSE below 0.5 dBA, dB in both cases. These models establish a fast and preliminary framework to assess noise impact from single UAV operations under realistic operational conditions.
- A reduced set of telemetry variables was found to be critical in predicting both metrics, with some similarities and differences in both sets of predictors. The Mach tip numbers of the upper and lower rotors coupled to the emission angle are key features for predicting the dynamics of both OSPL and OASPL. For OASPL, these variables

provide high accuracy by predicting the overall trends and some fast events. Thrust was also found to be important for increasing the representation of specific fast events, while including the vertical Mach number improves the prediction of middle-timescale events.
- For OSPL, the upper and lower Mach tip numbers are also essential parameters. The fact that a variable describing fluctuations on the flight dynamics improves predictions implies that part of the low-frequency OSPL fluctuations reflects perturbations to the average activity of the lower set of rotors.
- The relative performance of the OSPL and OASPL models differs significantly: OASPL predictions are more accurate and precise. OSPL exhibited larger and more frequent fluctuations than OASPL, implying that such fluctuations are low-frequency in nature. While the timing of sharp events is mostly captured in both metrics, their amplitudes are are mostly underestimated. This indicates that the input variables are adequate, however, the HGBR framework is limited in predicting the entire events.
- Coupling between emission angle and flight dynamics variables effectively predicted the time-dependent behavior of OSPL and OASPL during ascent, hover, and descent maneuvers. The emission angle provides a long-timescale modulation of both OSPL and OASPL signal. A simple coupling assumption (i.e. $\sin\theta$) suffices to predict the trend behavior with good accuracy, consistent with the observed dipolar radiation pattern of both OSPL and OASPL. However, sharp fast activities and middle-timescale variations require incorporating flight dynamics variables along with the emission angle.

These results indicate that the proposed empirical models can accurately predict OASPL and OSPL during real operations, while being also employed to identify and better understand key drivers for their predictions. These models can also be used as tools to assist in the development of first-principle theories as it presents empirical relations between flight dynamics and acoustic observables.

The model accuracies indicate that the assumption that flight dynamics reflects acoustic dynamics is well adequate, although the specific dB/dBA levels depend on the modeling framework. In this case, HGBR performs well for signals with moderate sharp events, as in OASPL, while some larger deviations are observed in this timescale when the amplitude of events is considerably larger, as in OSPL.

Although variations in wind speed during the operations are partly reflected in the telemetry variables, the present dataset does not establish the model's generalization capability across a wide range of meteorological conditions. In particular, variations in wind, temperature, and humidity across different days are very limited. Future work should therefore validate the model using measurements collected under a wider range of meteorological conditions to assess its robustness and transferability on these variables.

Finally, additional key maneuvers such as horizontal flights will be studied in the future using HGBR and the telemetry-based approach. This is performed using data from the same flight campaigns. These maneuvers were completely autopilot-controlled, which reduces the sources of uncertainty to the variations. The sound pressure levels at different bands will be explored to study the existence of specific drivers responsible for the time-dynamics at different frequency domains.

CRediT authorship contribution statement

Camilo I. Andino Cappagli: Writing – original draft, Visualization, Validation, Software, Methodology, Investigation, Formal analysis, Data curation, Conceptualization; **Alireza Amiri-Simkooei:** Writing – review & editing, Visualization, Supervision; **Mirjam Snellen:** Writing – review & editing, Visualization, Supervision, Software, Project administration, Methodology, Funding acquisition, Formal analysis.

Declaration of competing interest

The authors declare that they have no known competing financial interests or personal relationships that could have appeared to influence the work reported in this paper.

Acknowledgments

The authors are grateful to the EC for supporting the present work, performed within the REFMAP project, funded by the European Union's Horizon Europe research and innovation program under grant agreement no. 101096698 (REFMAP). This publication solely reflects the authors' view and neither the European Union, nor the funding Agency can be held responsible for the information it contains. The authors would also like to acknowledge Amy Morin and Dr. Salil Luesutthiviboon, and the team of Agent Fly Technologies for their logistical and technical assistance during and after the experimental campaigns.

Data availability

Data will be made available on request.

Supplementary material

Supplementary material associated with this article can be found in the online version at 10.1016/j.ast.2026.114154.

References

[1] G. Ling, N. Draghic, Aerial drones for blood delivery, Transfusion 59 (S2) (2019) 1608–1611.
[2] S.R. Bassolillo, E. D'Amato, M. Mattei, I. Notaro, Distributed navigation in emergency scenarios: a case study on post-avalanche search and rescue using drones, Appl. Sci. 13 (20) (11186) (2023).
[3] B. Schäffer, R. Pieren, K. Heutschi, J.M. Wunderli, S. Becker, Drone noise emission characteristics and noise effects on humans—a systematic review, Int. J. Environ. Res. Public Health 18 (11) (5940) (2021).
[4] S.A. Rizzi, D.L. Huff, D.D. Boyd, P. Bent, B.S. Henderson, K.A. Pascioni, D.C. Sargent, D.L. Josephson, M. Marsan, H.B. He, R. Snider, Urban air mobility noise: current practice, gaps, and recommendations, Technical Report, National Aeronautics and Space Administration, Langley Research Center, Hampton, VA. (2020).
[5] M.J.B. Lotinga, C. Ramos-Romero, N. Green, A.J. Torija, Noise from unconventional aircraft: a review of current measurement techniques, psychoacoustics, metrics and regulation, Curr. Pollut. Rep 9 (2023) 724–745.
[6] V.S. D. Kim, J. Ko, S. Lee, Stochastic analysis of a single-rotor to quantify the effect of RPS variation on noise of hovering multirotors, Appl. Acoust. 182 (108224) (2021).
[7] S. Palleja-Cabre, P. Chaitanya, P. Joseph, Acoustic and aerodynamic performance of co-axial contra-rotating rotors with unequal diameters, 30th AIAA/CEAS Aeroacoustics Conference, 2024. June 4–7, Rome, Italy.
[8] C.E. Tinney, J. Sirohi, Multirotor drone noise at static thrust, AIAA J. 56 (7) (2018) 2816–2826.
[9] F. Yunus, D. Casalino, F. Avallone, D. Ragni, Efficient prediction of urban air mobility noise in a vertiport environment, Aerosp. Sci. Technol 139 (108410) (2023).
[10] R. Zamponi, G. Gioli Torrione, V. Zůbek, E. Gallo, A. Zarri, C. Schram, Maneuvering drone noise investigation in a reverberant environment, J. Acoust. Soc. Am. 157 (2025) 4468–4481.
[11] H. Jiang, T. Zhou, R. Fattah, X. Zhang, Multi-rotor noise scattering by a drone fuselage, 25th AIAA/CEAS Aeroacoustics Conference (2019) 2586.
[12] A. Zarri, E. Dell'Erba, W. Munters, C. Schram, Aeroacoustic installation effects in multi-rotorcraft: numerical investigations of a small-size drone model, Aerosp. Sci. Technol 128 (107762) (2022).
[13] M. Roger, S. Moreau, Tonal-noise assessment of quadrotor-type UAV using source-mode expansions, Acoustics 2 (2020) 674–690.
[14] R.S. McKay, S.T. Go, S. Jung, M.J. Kingan, Noise from unmanned aerial vehicle contra-rotating propellers, J. Phys.: Conf. Ser. 1909 (012008) (2021).
[15] R.S. McKay, M.J. Kingan, S.T. Go, R. Jung, Experimental and analytical investigation of contra-rotating multi-rotor UAV propeller noise, Appl. Acoust. 177 (107850) (2021).
[16] F. Yunus, D. Casalino, G. Romani, M. Snellen, Efficient prediction of propeller noise in non-axial uniform inflow conditions, Aerosp. Sci. Technol 157 (109860) (2025).
[17] J.E. Ffowcs Williams, D.L. Hawkings, Sound generation by turbulence and surfaces in arbitrary motion, Phil. Trans. R. Soc. A A264 (1969) 321–342.
[18] J.E. Ffowcs Williams, D.L. Hawkings, Theory relating to the noise of rotating machinery, J. Sound Vib. 10 (1969) 10–21.
[19] T. Zhou, H. Jiang, B. Huang, Quad-copter noise measurements under realistic flight conditions, Aerosp. Sci. Technol. 124 (107542) (2022).

[20] C. Ramos-Romero, N. Green, A.J. Torija, C. Asensio, On-field noise measurements and acoustic characterisation of multi-rotor small unmanned aerial systems, Aerosp. Sci. Technol. 141 (108537) (2023).
[21] C.I. Andino Cappagli, A. Amiri-Simkooei, M. Snellen, Empirical models to describe UAV tonal dynamics during real operations, Proceedings of QuietDrones 2024 (2024) 8–11 September, Manchester, UK.
[22] R.M. Yupa Villanueva, R. Merino Martinez, C.I. Andino Cappagli, A. Altena, M. Snellen, Effect of unmanned aerial vehicle configurations on the acoustic and psychoacoustic signatures, Proceedings of the 30th International Congress on Sound and Vibration (ICSV), 2024. July 8–11, Amsterdam, the Netherlands.
[23] C.I. Andino Cappagli, A. Amiri-Simkooei, S. Luesutthiviboon, T. Meiser, A. Morin, M. Zajačík, M. Rollo, M. Snellen, Machine learning-based modelling of UAV noise metrics in real conditions, Forum Acusticum | Euronoise, 2025. Málaga, Spain.
[24] R. Merino-Martínez, P. Sijtsma, M. Snellen, T. Ahlfeldt, J. Antoni, C.J. Bahr, D. Blacodon, D. Ernst, A. Finez, S. Funke, T.F. Geyer, S. Haxter, G. Herold, X. Huang, W.M. Humphreys, Q. Leclere, A. Malgoezar, U. Michel, T. Padois, A. Pereira, C. Picard, E. Sarradj, J. Siller, D.G. Simons, C. Spehr, A review of acoustic imaging methods using phased microphone arrays, CEAS Aeronaut. J. 10 (2019) 197–230.
[25] T. Hastie, R. Tibshirani, J. Friedman, The Elements of Statistical Learning. Data Mining, Inference, and Prediction (2nd ed.), New York, Springer (2009) 337–384.
[26] V. Vapnik, The Nature of Statistical Learning Theory, New York, Springer (1995).
[27] L. Mason, J. Baxter, P. Bartlett, M. Frean, Boosting algorithms as gradient descent in function space, Adv. Neural Inf. Process. Syst. (12) (1999) 512–518.
[28] A. Altmann, L. Toloşi, O. Sander, T. Lengauer, Permutation importance: a corrected feature importance measure, Bioinformatics 26 (10) (2010) 1340–1347.